NASA/TM-20220007061

SWIR Star Tracking

Aaron J. Swank
Glenn Research Center, Cleveland, Ohio

May 2022

NASA STI Program . . . in Profile

Since its founding, NASA has been dedicated to the advancement of aeronautics and space science. The NASA Scientific and Technical Information (STI) Program plays a key part in helping NASA maintain this important role.

The NASA STI Program operates under the auspices of the Agency Chief Information Officer. It collects, organizes, provides for archiving, and disseminates NASA's STI. The NASA STI Program provides access to the NASA Technical Report Server—Registered (NTRS Reg) and NASA Technical Report Server—Public (NTRS) thus providing one of the largest collections of aeronautical and space science STI in the world. Results are published in both non-NASA channels and by NASA in the NASA STI Report Series, which includes the following report types:

- TECHNICAL PUBLICATION. Reports of completed research or a major significant phase of research that present the results of NASA programs and include extensive data or theoretical analysis. Includes compilations of significant scientific and technical data and information deemed to be of continuing reference value. NASA counter-part of peer-reviewed formal professional papers, but has less stringent limitations on manuscript length and extent of graphic presentations.

- TECHNICAL MEMORANDUM. Scientific and technical findings that are preliminary or of specialized interest, e.g., "quick-release" reports, working papers, and bibliographies that contain minimal annotation. Does not contain extensive analysis.

- CONTRACTOR REPORT. Scientific and technical findings by NASA-sponsored contractors and grantees.

- CONFERENCE PUBLICATION. Collected papers from scientific and technical conferences, symposia, seminars, or other meetings sponsored or co-sponsored by NASA.

- SPECIAL PUBLICATION. Scientific, technical, or historical information from NASA programs, projects, and missions, often concerned with subjects having substantial public interest.

- TECHNICAL TRANSLATION. English-language translations of foreign scientific and technical material pertinent to NASA's mission.

For more information about the NASA STI program, see the following:

- Access the NASA STI program home page at http://www.sti.nasa.gov

- E-mail your question to help@sti.nasa.gov

- Fax your question to the NASA STI Information Desk at 757-864-6500

- Telephone the NASA STI Information Desk at 757-864-9658

- Write to:
  NASA STI Program
  Mail Stop 148
  NASA Langley Research Center
  Hampton, VA 23681-2199

NASA/TM-20220007061

SWIR Star Tracking

Aaron J. Swank
Glenn Research Center, Cleveland, Ohio

National Aeronautics and
Space Administration

Glenn Research Center
Cleveland, Ohio 44135

May 2022

Acknowledgments

This work was supported by the National Aeronautics and Space Administration (NASA) Space Technology Mission Directorate through the Game Changing Development Program. The work was performed as part of the Integrated Radio and Optical Communication project at the NASA Glenn Research Center. This research has made use of the NASA/IPAC Infrared Science Archive, which is funded by the National Aeronautics and Space Administration and operated by the California Institute of Technology. This research has made use of the Infrared Telescope Facility, which is operated by the University of Hawaii under contract 80HQTR19D0030 with the National Aeronautics and Space Administration.

Level of Review: This material has been technically reviewed by technical management.

This report is available in electronic form at http://www.sti.nasa.gov/ and http://ntrs.nasa.gov/

SWIR Star Tracking

Aaron J. Swank
National Aeronautics and Space Administration
Glenn Research Center
Cleveland, Ohio 44135

Abstract

This work investigates the use of a star tracker that senses star light in the short wave infra-red wavelengths, specifically at the photometric H-band. The number of stars available for tracking and the corresponding photometric H-band magnitude is presented using information derived from the Two Micron All Sky Survey (2MASS) catalog. The probability of observing at least four stars in the star tracker's field of view (FOV) at a given H-band magnitude or brighter is also presented. Finally, a notional short wave infra-red (SWIR) star tracker design is presented using the parameters calculated for the expected number of stars observed at the corresponding magnitudes in the photometric H-band. The results for the SWIR star tracker indicate the potential for a reduced FOV as compared to the visible wavelengths and relaxed star magnitude sensing requirements.

I. Introduction

Commercial star trackers are currently available for visible band detection and are not as yet available for wavelengths covering the short wave infra-red (SWIR) wavelengths. SWIR focal plane arrays are commercially available for terrestrial applications and existing publications for SWIR star tracking appear to be focused on such applications [1], [2]. The terrestrial applications are motivated by atmospheric limitations (reduced absorption by the atmosphere in the SWIR near 1550nm) and by the potential for both daytime and nighttime operations. Terrestrial applications do not necessarily investigate the benefits of a SWIR tracker over a visible-band tracker for space applications. The application of SWIR focal plane arrays for star tracking is likely to be seen in future years as the application is thought to have been limited to date by the availability of space-rated SWIR detectors. Concept missions are already in formulation, which would utilize SWIR star trackers [3]. Therefore, it is desired to investigate what benefits, if any, a star tracker operating in the SWIR wavelengths, such as the J-H photometric band, would exhibit as compared to traditional visible-band star trackers. The effective accuracy of a star tracker improves as the number of stars occurring in the FOV are used in the calculation. In addition, the measurement accuracy is a function of the number of available photons or rather the signal to noise ratio (SNR) associated with the measurement. Thus, before a star tracker operating in the SWIR regime can be designed or the performance estimated, the properties relating to the available stars for use must be quantified. This includes the quantity of stars in a given FOV and the corresponding brightness magnitudes. This work quantifies the number of stars available for star tracking and the corresponding photometric H-band magnitude. Finally, this work presents the expected performance of a notional design for a star tracker using a detector sensitive to SWIR wavelengths by using the calculated star population parameters, which is then followed by a discussion on the presented results.

II. Methodology and Results

The fundamental measurement of a star tracker is the angle of arrival for each observed star. The angle of arrival is typically measured using a lens and the centroid location on a focal plane array. The centroiding accuracy is a function of the SNR, which for a star tracker is established by the number of photons incident on the detector from the observed star. The desired measurement, namely the star tracker derived attitude solution, is obtained by combining the measured angle of arrival for multiple stars. The attitude accuracy of any star tracker improves as the number of stars in the FOV increases. An attempt can be made to suggest an expected performance for a star tracker constructed with a detector sensitive in the SWIR by comparing the available star flux and the number of stars used in the attitude equation to those values corresponding to the visible wavelengths. Noting that Planck's black-body radiation law exhibits a power law decrease in available flux with an increase in wavelength, one might quickly conclude that a star tracker operating in the SWIR wavelengths would be inferior to that of one operating in the visible wavelengths due to the reduced number of available photons. As will be shown in this work, simply comparing the ratio of star flux values for the same magnitude star at the respective operating wavelength bands yields misleading results. Using information available for the corresponding star magnitudes in addition to the overall number of stars in the star tracker FOV (full cone angle) at the desired wavelengths is important for assessing the performance. Thus, in order to determine the expected performance of a point design SWIR star tracker, this work will present all-sky star availability information for stars which radiate in the SWIR wavelengths.

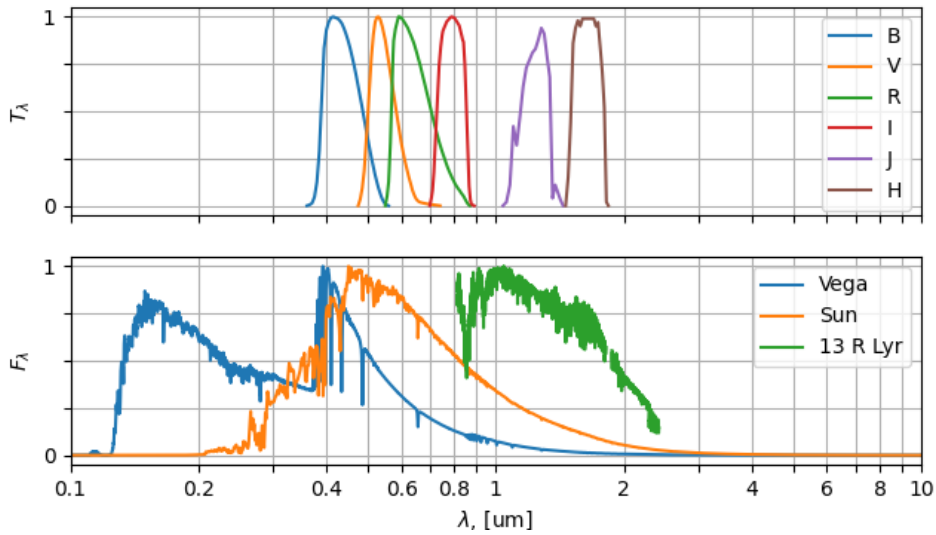

Fig. 1: Photometric spectral bands and normalized flux density. [5], [6], [7], [8], [9]

A. *Star Flux Comparison*

Centroiding accuracy using a pixelated focal plane detector is a function of the ratio of the incident signal to the sum of the squares of the noise contributions (SNR):

$$\mathrm{SNR} = \frac{\mathrm{Sig}}{\sqrt{S_n^2 + \mathrm{n_{px}} D_N t + \mathrm{n_{px}} N_r^2 + \mathrm{n_{px}} Q_n^2}} \tag{1}$$

where Sig is the total signal, S_n is the photon shot noise, D_N is the dark noise, N_r is the readout noise, Q_n is the quantization noise, $\mathrm{n_{px}}$ is the number of pixels used to measure the signal and t is the integration time. Due to the Poisson nature of the signal received on the detector, the shot noise is equal to the received signal. Assuming the measurement is shot noise dominated, the SNR becomes proportional to the square root of the signal:

$$\mathrm{SNR} = \frac{\mathrm{Sig}}{\sqrt{S_n^2}} = \frac{\mathrm{Sig}}{\sqrt{\mathrm{Sig}}} = \sqrt{\mathrm{Sig}} \tag{2}$$

Thus, in order to assess the relative impact on the centroiding accuracy, and hence star tracker accuracy, one may compare the square root of the computed star flux ratio between the visible and SWIR wavelengths.

Star catalogs are readily available, which tabulate star magnitudes at different photometric bands. Cataloged star magnitude reference values for each spectral band are specified relative to α Lyrae (Vega) by convention. Star magnitude is on a logarithmic scale, with larger numbers representing dimmer brightness. A number of photometric systems have been developed for characterizing star magnitudes. Calculations here are based on the Johnson-Cousins-Glass Photometric System [4], [5]. The optical flux is specified over specific, integrated spectral bands, as illustrated in Figure 1. For this work, the SWIR star tracker is assumed to operate in the J and H spectral bands, as these coincide with spectral response of InGaAs detectors. Clearly, the magnitude of a star will be different depending on the specified spectral band as the spectral emission of stars peak at different wavelengths. Figure 1 also depicts normalized star spectra for a visual depiction of how the calculated star magnitude relative to Vega will depend on the specified spectral band. As will be shown later, the distribution of star spectra yields more stars with greater magnitude in the H-band than the number of stars at the same magnitude in the V-band.

Individual band-integrated flux values were calculated using the flux density obtained from the online Magnitude to Flux Density converter tool [10] and then multiplied by the bandwidth to obtain the corresponding in-band flux. Table I lists the resulting in-band star flux for various star magnitudes which are then combined to determine the available flux across the wavelengths corresponding to a visible and a SWIR wavelength detector. By comparing the sum of the flux for the visible photometric bands listed in Table I with the sum of the J and H photometric bands for the SWIR regime, one obtains a flux ratio of visible to SWIR of approximately 13. Thus, there is approximately 13 times more flux available in the BVRI bands as compared to the JH bands for the same magnitude star. Therefore, the net result would be a $\sqrt{13}$ or approximately a factor of 3.6 worse in centroiding accuracy. Note that this calculations is an approximation as the entire flux incident on the detector is not accounted for, nor is the quantum efficiency of the detector included. Using this simplistic approach, some of the flux is not included, as there is a small gap between the J and H photometric band that is not accounted for by using the standard

Band	λ_{eff} [um]	λ_{bw} [um]	Flux, [W/m^2] x 10^{-12} m = 2	m = 3	m = 4	m = 5	m = 6
B	0.43	0.089	943	376	150	60	24
V	0.55	0.084	499	199	79	32	13
R	0.70	0.158	450	180	71	28	11
I	0.90	0.154	239	95	38	15	6
SUM B,V,R,I			2131	850	338	135	54
J	1.235	0.213	104	41	16	7	3
H	1.662	0.307	61	24	10	4	2
SUM J,H			165	65	26	11	5

TABLE I: Star flux for designated photometric bands at the corresponding star magnitudes, m, using star flux density values obtained from [10]. The photometric band center wavelength, λ_{eff}, and the corresponding total bandwidth, λ_{bw}, used to convert the flux density to flux values are listed for reference.

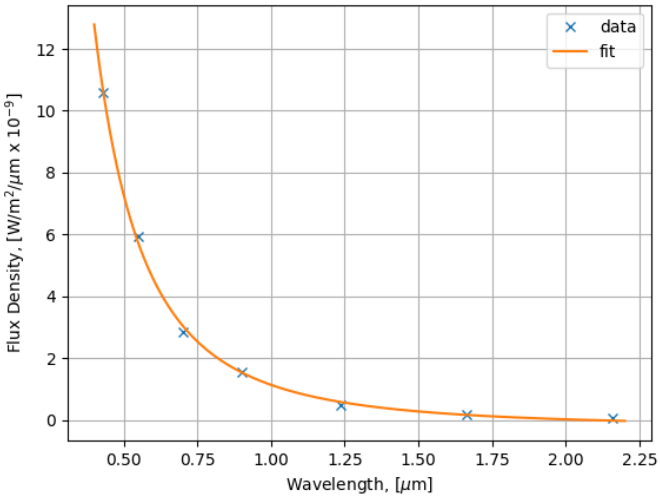

Fig. 2: Curve fit to magnitude 2 star flux density values obtained from [10]

photometric band width definitions. In addition, InGaAs detectors for sensing in the SWIR wavelengths are typically sensitive to approximately 900 nm, which is outside of the photometric J-band definition.

A slightly better approximation is obtained by integrating flux density curve for each of the respective detector spectral response wavelengths and then comparing the flux ratios. In order to get an approximation of total power on the detector across the detector bandwidth, one can approximate the flux density curve by fitting to an inverse power polynomial, consistent with Planck's blackbody radiation law that exhibits an inverse power relationship to wavelength. A curve fit to the flux density corresponding to a magnitude 2 star is shown in Figure 2, which may be used to estimate the total flux across the entire detector bandwidth. The integration limits are assumed to be 0.35 um to 1.0 um for the visible detector and 0.9 um to 1.8 um for the SWIR detector which is consistent with Si an InGaAs detectors. By integrating the flux density curve, a visible to SWIR flux ratio of 6.6 is obtained. The resulting centroiding accuracy would be expected to be equivalent to a factor of $\sqrt{6.6} = 2.6$ worse for the SWIR detector when using stars of the same magnitude in both the visible and SWIR bands.

B. Number of Available Stars for Tracking

The number of stars available in the star tracker FOV and the corresponding brightness magnitude affect the attitude estimate. Star tracker quaternion estimation algorithms (solution to Wahba's problem [11]) require at a minimum two vector measurements (two stars), and improved accuracy is obtained with multiple sources. The number of stars in the field of view is important as improved accuracy is obtained with multiple sources. Averaging of random errors improves the attitude estimate in the cross-boresight directions by a factor of $1/\sqrt{N_{\text{Stars}}}$ [12]. In addition, a minimum number of stars in the FOV must be met for the star tracker algorithms. For lost-in-space star identification and for averaging of random errors, it is desirable to track at least four stars. Attitude solutions near the galactic equator may be different from those near the galactic poles where there are fewer stars available for inclusion into the attitude solution. The evaluation of star magnitude occurrences is based on data obtained from the 2MASS Catalog [13], [14] and the Hipparcos Catalog [15], [16]. The 2MASS catalog contains stars around the two micron value, corresponding to the J and H photometric bands with 470,992,970 sources. The Hipparcos catalog has information cataloged for the visible photometric bands with 118,218 sources.

FOV:	3°	6°	12°
m_v = 3	–	0.1	0.5
m_v = 4	0.1	0.3	1.4
m_v = 5	0.3	1.0	4.0
m_v = 6	0.7	2.9	11.7

TABLE II: Empirical number of stars in FOV at visible star magnitudes. Ref [17], Eqn. 8.

FOV	3°	4°	5°	6°	8°	10°	12°
V-Band							
m_v = 3	–	–	0.1	0.1	0.2	0.3	0.4
m_v = 4	0.1	0.1	0.2	0.3	0.5	0.9	1.2
m_v = 5	0.2	0.4	0.6	0.9	1.7	2.7	3.9
m_v = 6	0.7	1.25	2.0	2.9	5.2	8.2	12.0
m_v = 7	2.2	3.9	6.1	8.9	16.0	25.4	36.9
m_v = 8	5.9	10.5	16.4	23.8	42.7	67.5	98.3
H-Band							
m_H = 2	0.3	0.5	0.7	1.1	1.9	3.0	4.4
m_H = 3	0.8	1.4	2.2	3.2	5.8	9.1	13.3
m_H = 4	2.3	4.1	6.4	9.3	16.7	26.4	38.5
m_H = 5	6.5	11.6	18.2	26.3	47.4	75.0	109.3
m_H = 6	18.7	33.5	52.7	76.3	137.4	217.7	317.8

TABLE III: Average number of stars in FOV, all-sky random search

Average and median star populations were obtained for a range of FOV using an all-sky search random search. In total, the average value is determined from 5e4 random iterations. For verification of the implemented method, calculation results are compared with the all-sky empirical relationship published by Liebe [17]. The empirical formula derived by Liebe establishes an average number of stars within a field of view given a star magnitude in the V-band and was developed using the PPM catalog [18], which has 378,910 sources. Values computed for the number of stars within a FOV using Liebe's empirical equation for visual magnitude, m_v, corresponding to the Johnson V-Band is given in Table II. Since the empirical equation is derived from a star catalog, the computed number of stars in the field of view corresponds to the number of *cataloged* stars in the FOV and may be different when applied to different star catalogs. It should also be noted, that the statistical properties for the observed number of stars in the FOV as determined for the V-band are not directly applicable for the stars observed at the SWIR wavelengths, as stars radiate in different parts of the spectrum with a peak flux centered at different wavelengths.

The results of the all-sky random search for the average number of stars in a given FOV for the visible, m_v, and the H-Band, m_H, is provided in Table III. The all-sky random search results for the visible band are consistent with the results in Table II as determined by the empirical equation. As shown in Table III, an equivalent number of stars within a given FOV for the H and V bands is achieved with larger FOVs at dimmer star magnitudes for the visible band. For instance to achieve an average of 9 stars in a six degree FOV, detection at $m_H = 4$ is necessary, while in the visible band detection at $m_v = 7$ is necessary.

Histograms for the number of stars observed at two specified FOVs at H-Band magnitudes three to five and brighter is shown in Figure 3. It is seen from the histograms that the distribution exhibits a heavy tail. The heavy tail skews the average value higher than the peak or median value. Table IV depicts a comparison of the average and median number of stars in a given FOV for specified magnitude stars and brighter. The difference between the median and average value is more prominent for dimmer stars. The observed characteristic is likely due to the significantly higher density of stars within the galactic plane. A plot of the stars with $m_H \leq 5$ in the J2000 coordinate frame is shown in Figure 4 with a clear depiction of the galactic plane, characterized by the increase in star density. In this work, the median number of stars in the FOV will be used rather than the average. In comparison, a method using an average star density value to estimate the number of available stars would yield a value with more stars in the FOV. When estimating the star tracker attitude performance, the result would be an optimistic reduction in the attitude error by $1/\sqrt{N_{\text{stars}}}$, as the average star density is skewed by the higher star density within the galactic plane.

FOV:	4°		5°		6°		7°		8°		9°		10°		11°		12°	
	Avg	Med	Avg	Med	Avg	Med	Avg	Med	Avg	Med	Avg	Med	Avg	Med	Avg	Med	Avg	Med
m_H = 2	–	–	–	–	1.1	1	1.4	1	1.9	2	2.4	2	3.0	3	3.7	3	4.4	4
m_H = 3	1.4	1	2.2	2	3.2	3	4.4	4	5.8	5	7.4	6	9.2	8	11.1	9	13.3	11
m_H = 4	4.1	3	6.4	5	9.3	7	12.8	9	16.9	12	21.4	16	26.7	20	32.4	24	38.5	29
m_H = 5	11.7	8	18.3	12	26.3	17	36.4	24	48.0	31	60.9	39	76.0	49	92.1	60	109.3	72
m_H = 6	33.9	19	53.0	29	76.3	42	105.4	58	139.2	77	176.5	98	220.3	122	267.2	150	317.8	180

TABLE IV: Average and median number of stars in FOV, all-sky random search

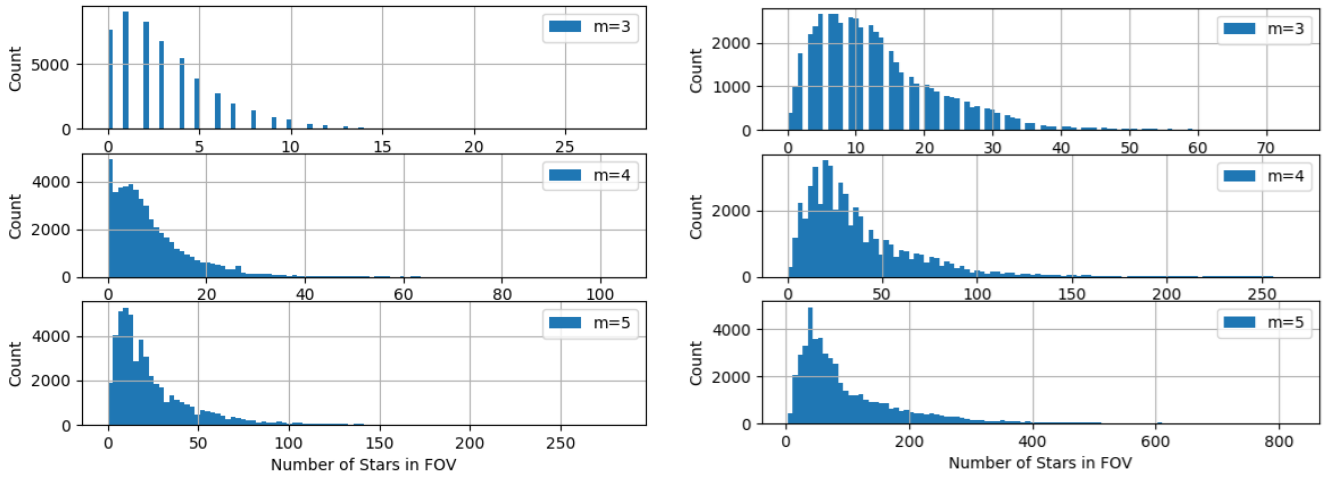

(a) 6 deg FOV

(b) 12 deg FOV

Fig. 3: Histogram depicting the number of stars in FOV at specified $\mathrm{m_H}$ magnitude and brighter.

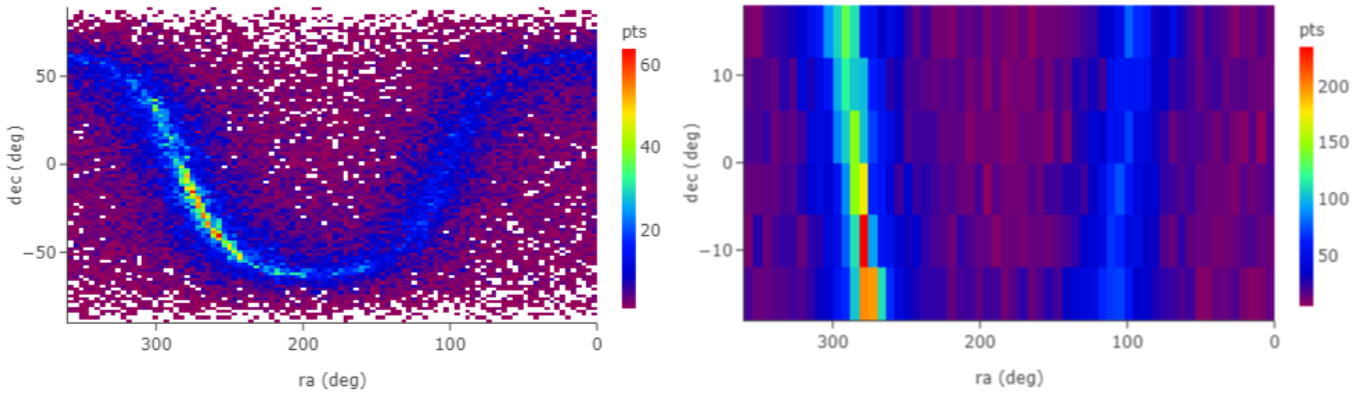

Fig. 4: (Left) All sky star count for stars at magnitude $\mathrm{m_H} = 5$ and brighter. (Right) Zoom of region within +/- 18 deg declination with bins of 6 x 6 deg of arc. [14]

C. Star Count Probability

A minimum number of stars in the FOV must be met for the star tracker algorithms. For example, lost-in-space algorithms such as Mortari's Pyramid Identification technique requires a minimum of four stars [19]. The probability of observing N stars or more within a given magnitude range and for a specified FOV is derived from the Hipparcos and the 2MASS catalogs for the visible and the H photometric bands respectively. The results for the visible band are found in Figure 5 and the results for the H-band are depicted in Figure 6. Similar to the results for the average number of stars within a given FOV, equivalent star occurrence probability values for the H-band are obtained at smaller values for the FOV at brighter star magnitudes. For example, a 90% chance of having at least 4 stars in the FOV with $\mathrm{m_H} \leq 4$ is obtained at an 8° FOV, whereas the equivalent star occurrence probability in the visible would require almost $\mathrm{m_v} \leq 7$ at the same FOV or alternatively $\mathrm{m_v} \leq 6$, at a 12° FOV.

III. Example SWIR Star Tracker

Presented here is a point-design example for a SWIR star tracker. This design is not in any way optimized, but rather is presented to provide an example of the SWIR star tracking approach and an understanding of the limitations. The design will be approached from a theoretical perspective and real-world as-built hardware is expected to exhibit reduced performance. For the point design analysis there are two cases to consider for performance estimation: 1) Star wavefront angle of arrival measurement via centroiding (Sec. III-A), and 2) Star tracker attitude determination (Sec. III-B). In order to provide a performance estimate for each of these conditions, realistic hardware parameters must be assumed. The SWIR star tracker point design assumes the parameters as specified in Table V.

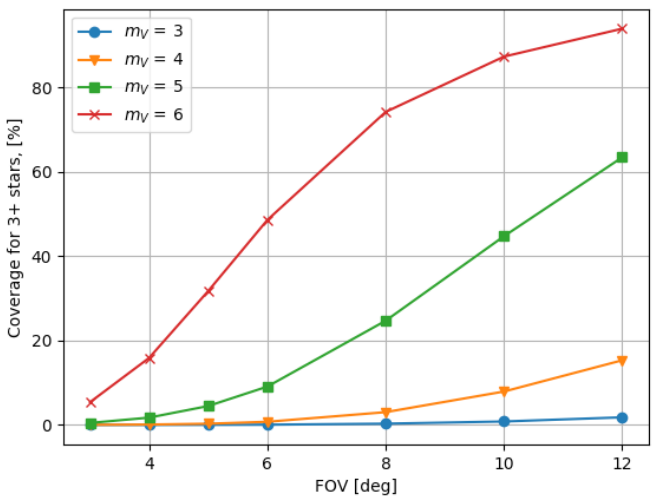

(a) 3+ Stars

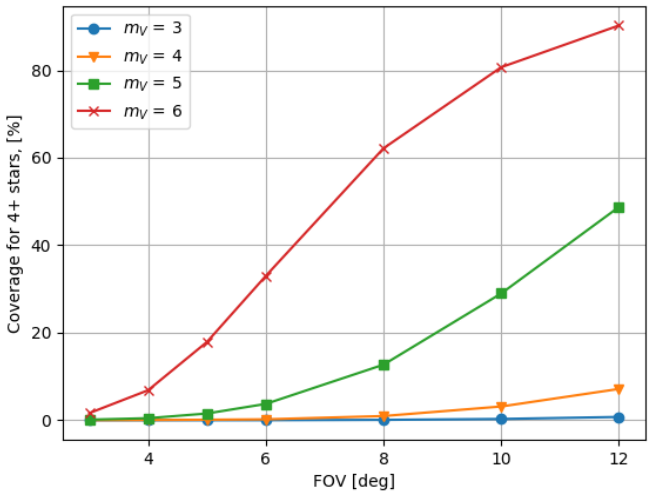

(b) 4+ Stars

FOV	3°	4°	5°	6°	8°	10°	12°
For 3+ Stars:							
$m_v \leq 3$	–	–	–	0.1	0.3	0.8	1.8
$m_v \leq 4$	–	–	0.3	0.7	3.0	7.9	15.3
$m_v \leq 5$	0.5	1.7	4.5	9.1	24.7	44.8	63.5
$m_v \leq 6$	5.4	15.9	31.8	48.6	74.3	87.4	94.0
$m_v \leq 7$	36.1	62.8	78.7	86.9	95.0	98.7	99.8
$m_v \leq 8$	78.1	89.3	94.3	97.1	99.7	100	100
For 4+ Stars:							
$m_v \leq 3$	–	–	–	–	0.1	0.3	0.7
$m_v \leq 4$	–	–	0.1	0.2	1.0	3.1	7.2
$m_v \leq 5$	0.1	0.5	1.5	3.7	12.7	29.0	48.8
$m_v \leq 6$	1.6	6.9	17.9	33.0	62.2	80.7	90.2
$m_v \leq 7$	21.4	48.5	69.6	81.2	92.1	97.4	99.5
$m_v \leq 8$	69.1	85.2	91.7	95.5	99.2	100	100

Fig. 5: All-sky star occurrence probability vs. FOV for various V-band magnitudes and brighter.

Specification	Value
Aperture size:	50 mm
FOV:	9 °
Focal Length:	100 mm

(a) Lens

Specification	Value
Size:	1280 x 1024 pixels
Pixel Pitch:	12.5 um
Noise (RMS):	25 electrons
Spectral response:	0.9 um to 1.7 um

(b) Focal Plane Array

TABLE V: Parameters for notional SWIR star tracker design.

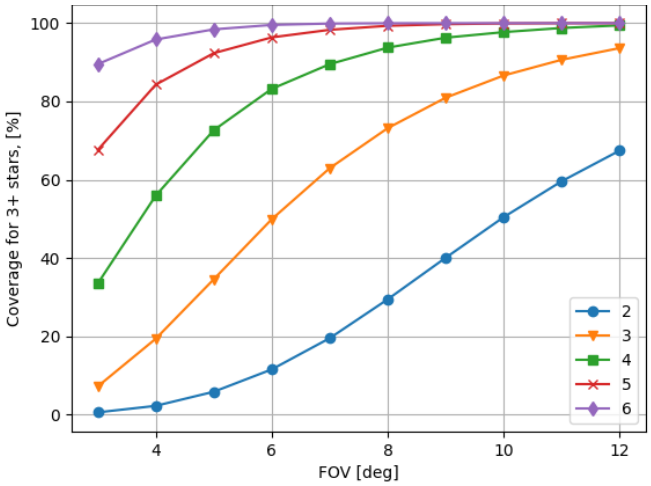

(a) 3+ Stars

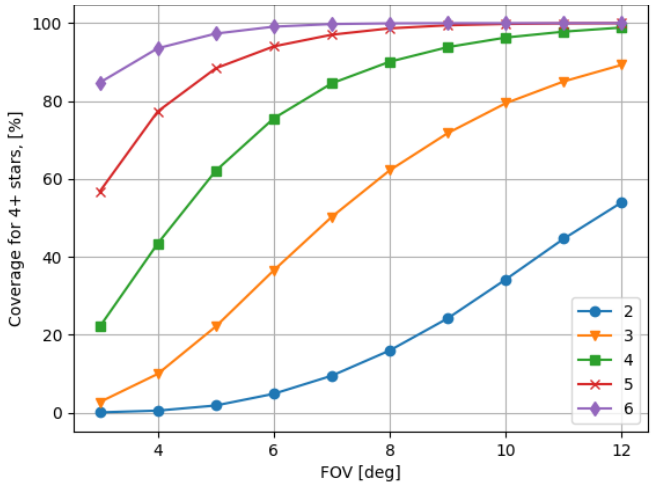

(b) 4+ Stars

FOV	3°	4°	5°	6°	7°	8°	9°	10°	11°	12°
For 3+ Stars:										
$m_H \leq 2$	0.6	2.2	5.8	11.5	19.5	29.5	40.1	50.5	59.6	67.5
$m_H \leq 3$	7.2	19.4	34.6	49.9	63.0	73.2	81.0	86.6	90.7	93.6
$m_H \leq 4$	33.5	55.9	72.7	83.2	89.5	93.8	96.3	97.7	98.8	99.4
$m_H \leq 5$	67.6	84.3	92.3	96.4	98.3	99.3	99.7	99.9	100	100
$m_H \leq 6$	89.5	95.8	98.4	99.6	99.9	100	100	100	100	100
For 4+ Stars:										
$m_H \leq 2$	0.1	0.5	1.9	4.9	9.5	16.0	24.2	34.2	44.7	54.0
$m_H \leq 3$	2.7	10.0	22.1	36.6	50.3	62.2	71.8	79.5	85.1	89.3
$m_H \leq 4$	22.1	43.4	62.1	75.6	84.6	90.1	93.9	96.3	97.8	98.9
$m_H \leq 5$	56.8	77.3	88.4	94.0	97.0	98.7	99.5	99.8	100	100
$m_H \leq 6$	84.7	93.6	97.3	99.1	99.8	100	100	100	100	100

Fig. 6: All-sky star occurrence probability vs. FOV for various H-band magnitudes and brighter.

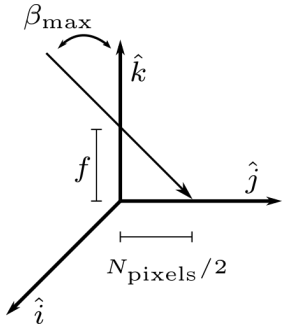

Fig. 7: Simplified star tracker geometry depicting the relationship between focal length f, number of pixels and FOV/2 = $\beta_{\max}$

A. *Centroiding Capability for Angle of Arrival Measurement*

A star tracker operates using the fundamental measurement of the star light angle of arrival. The standard technique is to use a pixel array with a lens such that the displacement on the focal plane array is related to the focal distance of the lens and the angle of arrival of the light. The geometry of this configuration is depicted in Figure 7. In order to measure the incoming angle of arrival, the centroid position on the focal plane array must be measured. The accuracy of the angle of arrival measurement is therefore dependent upon the ability to measure the centroid position on the focal plane array. A closed form solution and a Cramer-Rao lower bound (CRLB) estimate for the centroid error asymptotic solution, assuming only shot noise when spot size is larger than the pixel size is given by [20]:

$$\sigma_{\alpha_2} = \frac{\alpha_3}{2\sqrt{\alpha_1}} \tag{3}$$

where the alpha terms are non-dimensional quantities defined by:

α_1 = [photon count rate] * [integration time]
α_2 = [peak spot location on detector] / [pixel width]
α_3 = [imaged spot radius] / [pixel width]

Note that due to the nature of a Poisson distributed signal, the term α_1 is related to the SNR via: $\sqrt{\alpha_1} = \sqrt{\text{Sig}} = \text{Sig}/\sqrt{\text{Sig}} = \text{Sig}/\sqrt{S_n^2} = \text{SNR}$ for a shot noise dominated condition. The simplified expression in Equation 3 is valid for all α_3, when α_2 is equal to 0.5 (ie when the spot is located in the middle of the pixel). For a shot noise dominated signal, Equation 3 can be re-written as:

$$\sigma_{\alpha_2} = \frac{\alpha_3}{2\,\text{SNR}} \tag{4}$$

A plot of the closed form solution as a function of SNR values, Equation 4, is shown in Figure 8. From reference [20], the closed form solution results in a minimum error of 0.015 pixels (1/66th of a pixel) for an α_3 = 0.63, yielding an optimum spot diameter of 1.26 pixels. The Cramer-Rao lower bound is the lowest possible measurement error, assuming the only noise source is the Poisson noise associated with the detected signal (ie. shot noise dominated). Any real instrument will yield a higher error. A spot diameter on the order of 1.6 to 1.8 pixels is typical for star trackers, as optimal defocusing results in a point spread function width between 1.5 and 2 pixels [12], [21], [22]. As noted in [20], if the "shot noise is the dominant error source, then spreading the image over many pixels will produce accurate centroid estimates". In practice, a centroid position accuracy on the order of 1/10th of a pixel is considered simple, with advanced techniques under specialized conditions at 1/50th of a pixel. Commercial star trackers can achieve centroiding accuracy of 1/40th of a pixel or better. For the purposes here, it will be assumed that the practical centroiding limit is on the order of 1/40th to 1/50th of a pixel. Using Equation 4 one can estimate the required SNR. For 1/40th of a pixel centroiding capability, using a ratio of the spot diameter to pixel size on the order of 1.6 to 1.8, the required SNR is on the order of 16 to 18.

Using Equation 4 in combination with the expected star flux density at different magnitudes, one can establish the required star magnitude to meet the specified centroiding accuracy. Returning to Equation 1 and assuming a root mean squared (RMS) noise contribution, N_{RMS}, the SNR equation becomes:

$$\text{SNR} = \frac{\text{Sig}}{\sqrt{S_n^2 + \text{n}_{\text{px}} N_{\text{RMS}}^2}} \tag{5}$$

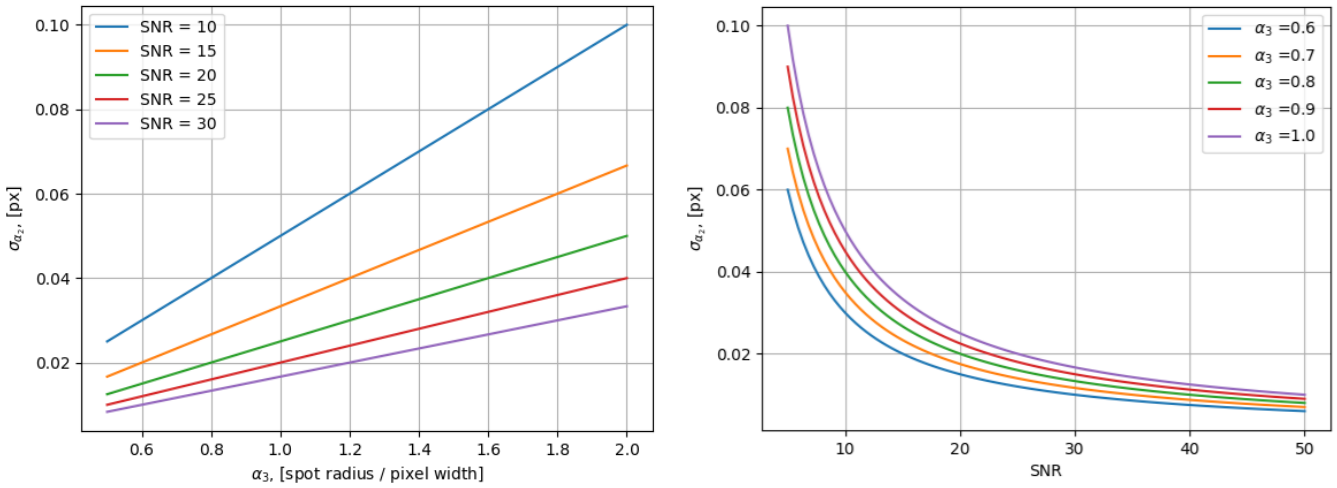

Fig. 8: Centroiding error; Left: versus the nondimensional particle image radius α_3, Right: versus SNR

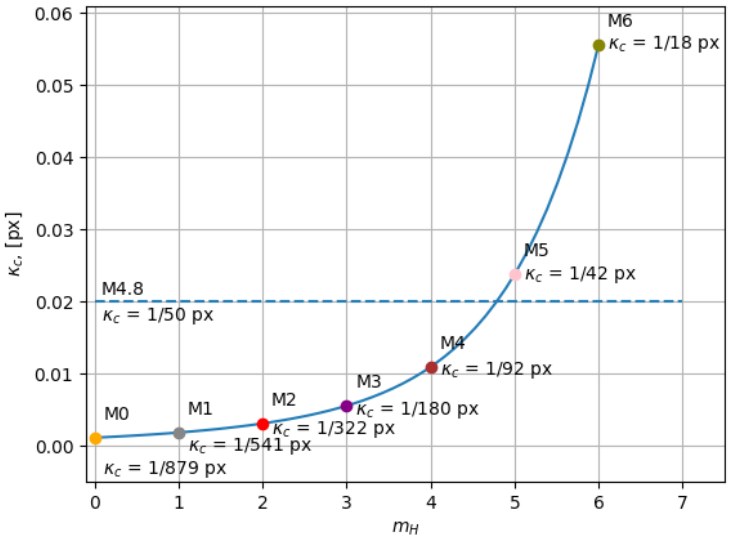

Fig. 9: Centroiding error, κ_c, as function of star magnitude. Centroiding errors better than 1/66th of a pixel are beyond the theoretical CRLB limit. Results are for a 50 mm aperture, with $\alpha_3 = 0.9$, N_{RMS} = 25 e-, and $\mathrm{n_{px}}$ = 9 px.

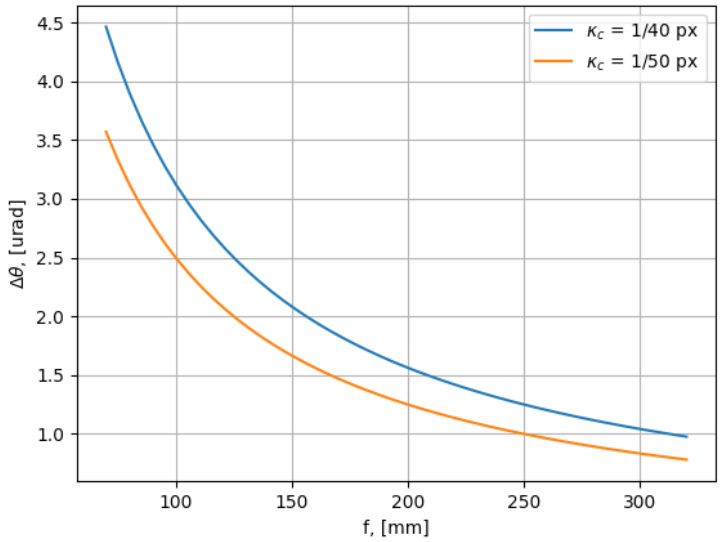

Fig. 10: Angular error as function of lens focal length for pixel pitch of 12.5 um and centroiding capabilities of 1/40th and 1/50th of a pixel.

In order to support measurement of a spot with a diameter to pixel size on the order of 1.6 to 1.8, it is assumed that 9 pixels, ie a 3x3 pixel grid, are used used for estimating the noise when calculating the signal to noise ratio. Using the specifications in Table V, the centroiding error (using Equation 4) can be plotted as a function of star magnitude as shown in Figure 9. Note that in Figure 9, the practical centroiding limit is reached for stars brighter than $\mathrm{m_H} = 4.8$ and no improvement beyond the theoretical limit of 1/66th of a pixel is feasible. A magnitude 5 star in the H-band corresponds to roughly the assumed 1/40th of a pixel centroiding capability. Thus, detection of stars at $\mathrm{m_H} = 5$ or brighter would be required and sensing of dimmer stars would require a larger aperture.

To establish the angular measurement resolution, one must determine a practical value for the pixel pitch. For InGaAs SWIR focal plane arrays, the pixel pitch is on the order of 12.5 um for commercial detectors (not necessarily those with space flight heritage). Example specifications listed in Table V are based on those published for the Sensors Unlimited InGaAs detector [23]. Since the angle of arrival is obtained by measuring a displacement on the focal plane array, the angular resolution also depends on the lens focal length. The relationship of the focal length to the angular error for a pixel pitch of 12.5 um is shown in Figure 10. Some caution must be noted when utilizing the results in Figure 10, as one can not simply increase the focal length in order to improve performance. As shown in Figure 7, changing the focal length for a fixed-sized detector specifies the FOV.

	FOV = 6°	FOV = 9°	FOV = 12°
$N_{\mathrm{stars}} = 4$:	$\Delta\theta_{\mathrm{c-b}}$ = 1.0 urad	$\Delta\theta_{\mathrm{c-b}}$ = 1.5 urad	$\Delta\theta_{\mathrm{c-b}}$ = 2.0 urad
$\mathrm{m_H} \leq 4$:	$N_{\mathrm{stars}} = 7$ P_{4+} = 75.6 % $\Delta\theta_{\mathrm{c-b}}$ = 0.773 urad	$N_{\mathrm{stars}} = 16$ P_{4+} = 93.9 % $\Delta\theta_{\mathrm{c-b}}$ = 0.767 urad	$N_{\mathrm{stars}} = 29$ P_{4+} = 98.9 % $\Delta\theta_{\mathrm{c-b}}$ = 0.759 urad
$\mathrm{m_H} \leq 5$:	$N_{\mathrm{stars}} = 17$ P_{4+} = 94.0 % $\Delta\theta_{\mathrm{c-b}}$ = 0.496 urad	$N_{\mathrm{stars}} = 39$ P_{4+} = 99.5 % $\Delta\theta_{\mathrm{c-b}}$ = 0.491 urad	$N_{\mathrm{stars}} = 72$ P_{4+} = 100 % $\Delta\theta_{\mathrm{c-b}}$ = 0.482 urad

TABLE VI: Summary of theoretical star tracker cross-boresight error, $\Delta\theta_{\mathrm{c-b}}$, using the median number of stars in a given FOV. For reference, the all-sky star occurrence probability for four or more stars in the specified FOV, P_{4+}, is listed.

For example, suppose it is desired to achieve a 1 urad angle accuracy and the focal length is increased to meet the desired performance. To achieve a 1 urad angle accuracy for a single star wavefront, at 1/40th of a pixel centroiding with the InGaAs detector having a 12.5 um pixel pitch capability, a focal length of 312 mm is needed (px * 1/40 = f * theta). Using the diagonal dimension, the resulting value of $\beta_{\max}$ for the 312 mm focal length is only 1.9 ° for a full cone FOV of 3.8 °. Such a small FOV is unlikely to generate a sufficient number of stars in the FOV for an attitude solution. For the InGaAs pixel pitch of 12.5 um with a sensor of 1280 x 1024 pixels, a practical limit may be set on the FOV based on the limitation of the number of stars in the FOV and the probability of having sufficient stars for an attitude solution. Based on the information provided in Figure 6, a lower limit on the FOV is likely on the order of 6 ° FOV to 9 ° FOV depending on the sensed star magnitude and required star occurrence probability. A practical upper limit on the focal length for this configuration is therefore likely between 100 mm and 150 mm.

B. Star Tracker Attitude

The star tracker attitude calculation uses the wavefront angle of arrival measurement for multiple stars. The performance of a centroiding style star tracker is limited by the centroiding error and the CRLB estimates the maximum performance. Thus, single star or unit vector angular error is specified by the lens focal length, the pixel pitch, and the centroiding error. Simplified, theoretical relations for the attitude accuracy of a centroiding star tracker is given in reference [12]:

$$\Delta\theta_{\mathrm{cross-boresight}} = \frac{2\,\kappa_{\mathrm{c}}\,\beta_{\max}}{N_{\mathrm{pixels}}\sqrt{N_{\mathrm{stars}}}} \tag{6}$$

$$\Delta\theta_{\mathrm{roll}} = \frac{\sqrt{6}\,\kappa_{\mathrm{c}}}{N_{\mathrm{pixels}}\sqrt{N_{\mathrm{stars}}}} \tag{7}$$

where κ_{c} is the centroiding accuracy in fractions of a pixel, $\beta_{\max}$ is the max half cone angle of the optical field of view, (FOV/2). The simplified model is valid when the FOV/2 satisfies the small angle assumption, since in Equation 6, the focal length is specified by $(N_{\mathrm{pixels}}/2)\,/\beta_{\max}$, which is given in units of pixels. The simplified model scales by the square root of the number of stars in the field of view. Since the centroiding error is typically a function of signal to noise ratio, Equations 6,7 indirectly assume that all of the stars in the field of view are of the same centroiding error. As shown in Figure 9, a 1/50th pixel centroiding limit can be met at a $\mathrm{m_H} = 4.8$ for a 50 mm aperture. As such, the multi-star attitude estimation performance of the star tracker is easily estimated using Equation 6. All of the stars, regardless of magnitude brighter than $\mathrm{m_H} = 4.8$, will exhibit similar angular error.

For the attitude performance estimate, it is assumed that the uncertainty in the angle of arrival measurement is set by an optimistic centroiding error of 1/40th of a pixel. Using Equation 6 with a 9 ° FOV ($f \approx 100$ mm) and a 1280 pixel array, the resulting theoretical star tracker performance is on the order of 1.5 urad for the worst case of 4 stars available in the field of view. Assuming that all the stars in the FOV are of $\mathrm{m_H} = 4$ or brighter, the median number of stars in the FOV as listed in Table IV is 16, resulting in a performance of approximately 0.8 urad for the cross-boresight axes. The theoretical cross-boresight error is computed for other configurations and presented in Table VI. It is interesting to note, that while an increase in the star tracker FOV results in an increase in the median number of stars observed, the resulting cross-boresight error does not change significantly due to the increase in the single star angular error measurement associated with the reduced lens focal length.

IV. Discussion

A star tracker is limited in performance by the single star angle of arrival measurement estimate, which is set by the centroiding accuracy. While the centroiding accuracy is a function of the signal to noise ratio, optimal centroiding accuracy is necessary for the dimmest magnitude star that is to be observed and used in the attitude solution. If additional stars used in the computation are of dimmer magnitude, there is a corresponding higher associated measurement error. Incorporation of

these stars with a lower brightness (and reduced centroiding accuracy) into the attitude solution does not necessarily improve the attitude estimate due to the inverse weighting of the contribution by the variance in the angular estimate. Increasing the number of stars in the field of view with similar measurement accuracy improves the attitude estimate in the cross-boresight directions by a factor of $1/\sqrt{N_{\mathrm{Stars}}}$. Yet, simply increasing the FOV for a fixed-size focal plane array reduces the single star angle of arrival measurement accuracy. Thus, for a fixed-size focal plane array, increasing the FOV primarily improves the probability of having sufficient number of stars to obtain an attitude solution. The results in Table VI shows that increasing the FOV results in similar cross-boresight performance, but with a higher probability of viewing four or more stars in the FOV. As shown in Section II, the equivalent star occurrence probability for the H-band is obtained at smaller values for the FOV at brighter star magnitudes as compared to the visible band.

Star tracker designs utilizing reduced FOVs may allow simpler lens designs. For example, there is a trade-off between focal length and FOV as described in reference [24]. Increasing the FOV leads to a decrease in the focal length. Decreasing the F# and increasing the entrance aperture size increases the lens weight and length. Also, an increase in the FOV typically requires a more complicated lens design to reduce chromatic aberrations. Chromatic aberration will lead to a shift in the measured coordinates due to the shift in effective wavelength for stars with different spectra [25]. An increase in the FOV also has implications on the star tracker availability. Typically a star tracker is unable to operate when the sun is within the FOV. Depending on the baffle design, there is an angular keep-out zone larger than the star tracker FOV for the sun incident angle relative to the star tracker pointing direction. As a result, with an increased FOV, there is a reduction in the operational up-time for when the star tracker can generate a full performance solution due to the relative sun angles. A reduced FOV is therefore desired to increase operational up-time by allowing the star tracker to operate at smaller angles relative to bright objects in the sky such as the Sun, Earth or Moon. Reference [26], shows for example a reference mission where a star tracker with a 6° FOV provides an 85 % mission operation uptime as compared to 55 % uptime at 18° FOV.

The attitude estimate can be improved by increasing the number of stars used in the computation. For a fixed FOV, increasing the number of stars available for computing the attitude solution is achieved by sensing stars at dimmer magnitudes. As shown in Section II, the equivalent average number of stars within a given FOV in the H-Band is obtained at smaller FOVs and at brighter star magnitudes as compared to star tracking at the visible wavelengths. Using the results in Section II, in order to achieve an equivalent number or stars in a given FOV, the visible wavelengths require sensing at approximately three magnitudes dimmer as compared to the H-Band. For example, a visible magnitude of approximately magnitude $\mathrm{m_v} \leq 7$ yields similar values as for magnitude $\mathrm{m_H} \leq 4$. Clearly, a star tracker which may operate without the requirement of sensing very dim magnitude stars is advantageous for a number of reasons and a star tracker sensing at the H-band may result in a reduction in the required range of star magnitudes to be sensed.

The parameters for the focal plane array and and lens in the point design for the SWIR star tracker are similar to those available for visible star trackers. As a result, the performance estimates would be similar to the two devices assuming they are each optimized for the best SNR for angle of arrival measurement and centroiding accuracy. An advantage of sensing in the H-Band is a potential for a reduced FOV as compared to the visible wavelengths and without the requirement of sensing very dim magnitude stars.

V. Conclusion

To the knowledge of the authors, currently a space-rated commercial off the shelf SWIR star tracker is non-existent. An advantage of sensing in the H-Band for star tracking applications is the potential for a reduced FOV as compared to the visible wavelengths and relaxed star magnitude sensing requirements. As compared to star tracking at the visible wavelengths, the equivalent average number of stars within a given FOV in the H-Band is obtained at smaller FOVs and at brighter star magnitudes. Similarly, equivalent star occurrence probability values for the H-band are obtained at smaller values for the FOV at brighter star magnitudes.

The median number of stars in a given FOV was used to estimate the expected star tracker performance rather than using an average value for the all-sky star density. When computing the attitude performance, the average number of stars in the FOV was found to yield optimistic results due to influence of the increased star density near the galactic equator. The one-sigma angular error estimates for measuring the star wavefront angle of arrival and the multi-star attitude estimate was presented for an example star tracker design. The design assumed a 9° FOV ($f \approx 100$ mm) and a 1280 pixel, 12.5 um pitch SWIR focal plane array. The expected theoretical performance limit was found to be on the order of, 1.5 urad to 0.5 urad when sensing stars at magnitude in the H-Band of approximately $\mathrm{m_H} = 4-5$ or brighter. For the 9° FOV design, the probability of viewing four or more stars in the FOV at $\mathrm{m_H} \leq 5$ was found to be 99.5 % while sensing at $\mathrm{m_H} \leq 4$ was found to be 93.9 %. The star tracker performance estimates are theoretical and are likely optimistic as compared to actual as-built hardware.

REFERENCES

[1] Gudmundson, K., *Ground Based Attitude Determination Using a SWIR Star Tracker*, Master's thesis, Linköping University, 2019.

[2] Wang, W., Wei, X., Li, J., and Zhang, G., "Guide star catalog generation for short-wave infrared (SWIR) All-Time star sensor," *Review of Scientific Instruments*, Vol. 89, No. 7, 2018, pp. 075003.

[3] Swank, A. J., Aretskin-Hariton, E., Le, D. K., Sands, O., and Wroblewski, A., "Beaconless Pointing for Deep-Space Optical Communication," *34th AIAA International Communications Satellite Systems Conference*, 2016.

[4] Johnson, H. L. and Morgan, W., "Fundamental stellar photometry for standards of spectral type on the revised system of the Yerkes spectral atlas," *The Astrophysical Journal*, Vol. 117, 1953, pp. 313.

[5] Bessell, M. S., "Standard photometric systems," *Annu. Rev. Astron. Astrophys.*, Vol. 43, 2005, pp. 293–336.

[6] Infrared Telescope Facility, which is operated by the University of Hawaii under contract 80HQTR19D0030 with the National Aeronautics and Space Administration.

[7] Cushing, M. C., Rayner, J. T., and Vacca, W. D., "An infrared spectroscopic sequence of M, L, and T dwarfs," *The Astrophysical Journal*, Vol. 623, No. 2, 2005, pp. 1115.

[8] Rayner, J. T., Cushing, M. C., and Vacca, W. D., "The infrared telescope facility (IRTF) spectral library: cool stars," *The Astrophysical Journal Supplement Series*, Vol. 185, No. 2, 2009, pp. 289.

[9] Fouesneau, M., "pyphot – A tool for computing photometry from spectra," 2022.

[10] "NASA/IPAC Infrared Science Archive, Magnitude/Flux Density Converter." Online, Accessed April 2022: https://irsa.ipac.caltech.edu/data/SPITZER/docs/dataanalysistools/tools/pet/magtojy.

[11] Wahba, G., "A least squares estimate of satellite attitude," *SIAM review*, Vol. 7, No. 3, 1965, pp. 409–409.

[12] Markley, F. L. and Crassidis, J. L., *Fundamentals of spacecraft attitude determination and control*, Springer, 2014.

[13] Skrutskie, M. F., Cutri, R. M., Stiening, R., Weinberg, M. D., Schneider, S., Carpenter, J. M., Beichman, C., Capps, R., Chester, T., Elias, J., Huchra, J., Liebert, J., Lonsdale, C., Monet, D. G., Price, S., Seitzer, P., Jarrett, T., Kirkpatrick, J. D., Gizis, J. E., Howard, E., Evans, T., Fowler, J., Fullmer, L., Hurt, R., Light, R., Kopan, E. L., Marsh, K. A., McCallon, H. L., Tam, R., Dyk, S. V., and Wheelock, S., "The Two Micron All Sky Survey (2MASS)," *The Astronomical Journal*, Vol. 131, No. 2, feb 2006, pp. 1163–1183.

[14] NASA/IPAC Infrared Science Archive, which is funded by the National Aeronautics and Space Administration and operated by the California Institute of Technology.

[15] European Space Agency, "The Hipparcos and Tycho Catalogues," 1997, ESA SP-1200.

[16] Perryman, M., Lindegren, L., Kovalevsky, J., Hoeg, E., Bastian, U., Bernacca, P., Crézé, M., Donati, F., Grenon, M., Grewing, M., et al., "The HIPPARCOS catalogue," *Astronomy and Astrophysics-A&A*, Vol. 323, No. 1, 1997, pp. 49–52.

[17] Liebe, C. C., "Accuracy performance of star trackers-a tutorial," *IEEE Transactions on aerospace and electronic systems*, Vol. 38, No. 2, 2002, pp. 587–599.

[18] Roeser, S. and Bastian, U., *PPM star catalogue : positions and proper motions : J2000.0*, Published for Astronomisches Rechen-Institut by Spektrum Akademischer Verlag, Heidelberg; New York, 1991-1993.

[19] Mortari, D., Samaan, M. A., Bruccoleri, C., and Junkins, J. L., "The Pyramid Star Identification Technique," *Navigation*, Vol. 51, No. 3, 2004, pp. 171–183.

[20] Wernet, M. P. and Pline, A., "Particle displacement tracking technique and Cramer-Rao lower bound error in centroid estimates from CCD imagery," *Experiments in Fluids*, Vol. 15, No. 4, 1993, pp. 295–307.

[21] Salomon, P. M. and Glavich, T. A., "Image signal processing in sub-pixel accuracy star trackers," *Smart sensors II*, Vol. 252, International Society for Optics and Photonics, 1980, pp. 64–74.

[22] Secroun, A., Lampton, M., and Levi, M., "A high-accuracy, small field of view star guider with application to snap," *Experimental Astronomy*, Vol. 12, No. 2, 2001, pp. 69–85.

[23] Sensors Unlimited, C. A., "Mini-SWIR 1280JSX High Definition Camera," Online, Accessed April 2022.

[24] Asadnezhad, M., Eslamimajd, A., and Hajghassem, H., "Optical system design of star sensor and stray light analysis," *Journal of the European Optical Society-Rapid Publications*, Vol. 14, No. 1, 2018, pp. 1–11.

[25] Tuchin, M., Biryukov, A., Nickiforov, M., Prokhorov, M., and Zakharov, A., "On random and systematic errors of a star tracker," *27th Annual AIAA/USU Conference on Small Satellites*, 2013.

[26] Aretskin-Hariton, E., Swank, A., and Gray, J. S., "Beaconless Optical Communication System Constraints," *AIAA Scitech 2019 Forum*, 2019.